ASCE Journal of Environmental Engineering

Transport of Single-Layered Graphene Oxide Nanosheets through Quartz and Iron Oxide Coated–Sand Columns

Thomas A. Duster, Chongzheng Na, Diogo Bolster, and Jeremy B. Fein

DOI: 10.1061/(ASCE)EE.1943-7870.0001156

Supplemental Data

SLGO Nanosheet Synthesis and Characterization

Single layered graphene oxide (SLGO) nanosheets were synthesized from natural flake graphite (Alfa Aesar, 99.9995%) using the method of Hummers and Offeman (1958). Graphite was mixed with $NaNO_3$, concentrated H_2SO_4, and $KMnO_4$ in an ice bath. The mixture was then transferred to a water bath at 35 °C and stirred for 30 minutes. Next, ultrapure water (R>18 MΩ cm, TOC < 2 μgC L^{-1}) was added and the mixture was stirred for approximately 20 minutes. Residual permanganate was then consumed by the addition of hydrogen peroxide. Finally, the oxidized graphite was collected by centrifugation, washed/rinsed repeatedly with 1.2N HCl and ultrapure water, and freeze-dried under vacuum for 5 to 7 days before use. The resulting dried mass was then dispersed in ultrapure water using end-over-end rotation. The suspension was sonicated (40kHz) in a water bath for one hour and subsequently centrifuged in multiple 15 mL aliquots for 10 minutes at 3000 × g, which served to sediment the multi-layered graphene oxide aggregates and concentrated the SLGO nanosheets in the supernatant. All supernatants were decanted and combined into a single stock suspension with a final concentration of 2.1 g SLGO L^{-1}, as determined from the average difference between the wet and dried (105 °C for > 24 hours) masses of multiple 20 mL aliquots of the final suspension. We conducted all subsequent characterization and transport experiments using this stock SLGO suspension or its dilution.

SUPPLEMENTAL DATA

We characterized the physical and electrochemical properties of the SLGO nanosheets utilized in subsequent transport experiments using atomic force microscopy (AFM), dynamic light scattering (DLS), UV-visible (UV-vis) spectrophotometry, and electrophoretic mobility (EPM) measurements. Prior to examination by AFM (XE-70, Park Systems, Santa Clara, CA), an aliquot of the SLGO stock suspension was diluted 1:4 with ethanol and deposited on freshly cleaved mica. The instrument was operated in non-contact mode and images were flattened using the WSxM software package from Nanotec Electronica S.L. (Madrid, Spain). The AFM analyses resulted in determination of z-dimension, or height, which we used to infer the extent of exfoliation present in the SLGO nanosheet suspension. Figure 1 in the main text depicts representative non-contact AFM images from a dilution of the SLGO nanosheet suspension utilized for subsequent transport experiments. The images indicate that the SLGO nanosheets exhibit relatively flat and irregular morphology, consistent with the character of other SLGO nanosheets in the literature (Chen et al. 2009; Gao et al. 2009). SLGO nanosheets in this study exhibited a heterogeneous size distribution in terms of particle length and width, measuring from several hundred nanometers to approximately 1.5 μm in diameter (Figure 1a,b). However, SLGO heights generally ranged between 1.0 and 1.5 nm (Figure 1c), which is indicative of single-layered nanosheets (Park and Ruoff 2009; Zhang et al. 2010). Hence, the SLGO nanosheets utilized in this study exhibited extraordinary anisotropy, which is expected to play a significant role in their transport through porous media.

Prior to each transport study, we obtained a UV-vis absorption spectrum (λ = 200-800 nm; 6Q quartz cuvette) from the initial 25 mg SLGO L^{-1} suspension that was delivered to the packed column and obtained several additional spectra from the column effluent during the study (Figure S1). Regardless of the ionic strength and pH conditions of the background electrolyte, all UV-vis

spectra from the initial stock suspensions were in general agreement with each other and exhibited a peak absorbance between $\lambda = 230$ and 232 nm and a distinctive shoulder feature around 300 nm, which is characteristic of SLGO nanosheets and consistent with similar analyses in the literature (Li et al. 2008; Zhang et al. 2010; Gao et al. 2012). UV-vis spectra from effluent suspensions exhibited lower peak heights, as expected to indicate a change in SLGO concentration, but were otherwise identical to the spectra from the pre-column stock suspension (Figure S1, inset). The consistency between pre-column and post-column UV-vis spectra indicates the absence of chemical transformations (e.g., reduction; Li et al. 2008) or contamination of SLGO nanosheets within the column. This observation, combined with the linearly-proportional relationship between SLGO concentration and the absorbance of an SLGO suspension at $\lambda = 230$ nm (Figure S2), indicate that tracking UV-vis absorbance in the column effluent is a robust measure of SLGO transport through quartz and iron oxide coated sands and we utilized this metric to monitor breakthrough of SLGO nanosheets during the column transport studies.

Finally, for each ionic strength evaluated during the transport studies (10 mM and 50 mM), we measured EPM (Zetasizer Nano-ZS, Malvern Instruments, Worcestershire, United Kingdom) along a gradient of pH values between approximately pH 5.5 and pH 8.5 (~0.4 s.u. resolution). Separately, DLS measurements were also obtained at pH 5.6, 7.0, and 8.3. For each study, ionic strength was buffered by adding an appropriate mass of $NaClO_4 \bullet H_2O$ powder (Fisher Scientific; ACS grade) to a 25 mg SLGO L^{-1} suspension, while pH was titrated upwards with serial NaOH additions. Aliquots from the titrated suspension were removed and measured after between 5 (EPM) and 20 (DLS) minutes of exposure time at the target pH. The results of the DLS and EPM titrations are described in the main text.

POROUS MEDIA PREPARATION AND CHARACTERIZATION

Acid washed quartz sand (Accusand, Unimin Corporation, LeSueur, MN) was utilized as the solid phase medium for all uncoated sand column experiments and as the base grain for all iron oxide coated sand column experiments. Supplier specifications indicate that the quartz sand passed through the openings of a 40 mesh sieve (0.42 mm) while being retained on a 50 mesh sieve (0.29 mm), which defines the range of potential grain sizes. Quartz sand was sonicated and rinsed with ultrapure water approximately ten times to remove loosely-associated colloidal debris and soaked overnight in 10% HCl on two occasions to remove metal contaminants. After each overnight acid wash, the quartz sand was rinsed thoroughly with ultrapure water until the rinsate returned to circumneutral pH.

Iron oxide coated sand grains were produced similar to the procedure of Ams et al. (2004) by adding 150 g of the acid-washed quartz sand to each of two 600 mL beakers containing a 400 mL solution of 0.05 M $Fe(NO_3)_3 \bullet 9H_2O$ (Sigma-Aldrich; ACS grade). While stirring vigorously, the suspension was slowly titrated using 6 M NaOH until the pH exceeded 6.0. At this point, precipitation of an iron oxyhydroxide was observed on the quartz grains and after 3 hours of vigorous stirring, the entire suspension was transferred to capped polypropylene bottles and rotated end-over-end overnight. After settling the sand in these containers and decanting the supernatant, the sand was rinsed with ultrapure water, which liberated iron oxide precipitates that were not adhered to a sand grain. We repeated this rinse step over 20 times, at which time the UV-Vis absorbance of the rinsate was less than 0.05 at all points between λ = 200 and 800 nm. The iron oxide coated sand was oven-dried at 60 °C for approximately 12 hours. The rinsed and dried iron oxide coated sand was distinctly reddish-brown in color.

Morphological and chemical characteristics of individual grains from the quartz and iron oxide coated sands were established via scanning electron microscopy (SEM; Leo-EVO 50, Carl Zeiss, Oberkochen, Germany) coupled to an energy dispersive X-ray spectrometer (EDX; Oxford Instruments, Oxfordshire, United Kingdom). Figure S3 presents SEM images for representative quartz sand and iron oxide coated sand grains. Both grain types appear heavily coated with colloidal material; however, EDX spectroscopy measurements confirm the presence of an iron-bearing coating on the iron oxide coated sands, whereas quartz sands are only comprised of the elements silicon and oxygen. These measurements indicated a significant amount of iron oxide precipitate was present at the sand surface after only one coating. In order to facilitate direct comparison between the quartz and iron oxide coated sand experiments, we opted against conducting additional coatings that could increase the grain size and hence change the pore geometries of the solid phase matrix, relative to the pure quartz sand.

In addition, surface associated colloidal material was collected from the quartz and iron oxide coated sand grains via probe sonication (using a total cycle time of 20 minutes at 39 W) and vigorous vortexing (3200 rpm), respectively, and this material was subjected to an EPM titration, as described earlier for the SLGO suspensions. We assume that the near-surface charge of a sand grain is largely determined by the surface associated colloidal material (Jaisi et al. 2008; Smith et al. 2008). The relatively mild procedure for collecting colloidal material from the iron oxide coated sands protected the resulting suspension from contamination with colloidal silica from the underlying sand grain. The results from the EPM titrations are described in the main text.

All SLGO transport studies were conducted using borosilicate glass columns (FlexColumn, Kimble-Kontes Scientific) measuring 10.0 cm long by 1.0 cm in diameter. For both quartz sand and iron oxide coated sand experiments, 8.0 g of material was rinsed twice with ionic strength

buffer and ultrapure water (R>18 MΩ cm, TOC < 2 μgC L-1) to remove loosely-associated colloidal material, and then slowly added to a column prefilled with ultrapure water. The sand was settled by vigorously vibrating and tapping the filled columns, and excess water was removed using a pipette. Fresh quartz sand and iron oxide coated sand was packed into each column prior to the start of an experimental run. By carefully tracking the mass of the empty and the packed column, we established that the columns packed with either the quartz sand or iron oxide coated sands exhibited an average pore volume of 1.61 mL (σ = 0.03 mL). The height of sand within each column was a constant 6.0 cm throughout all experimental treatments. Combined, these values result in an average calculated porosity of 0.34 for each experimental system, which is in the range of typical porosities for natural sand-dominated system. All phases of the column transport studies described in the main text were conducted using an influent flow rate of 1 mL min^{-1} driven by a peristaltic pump, which resulted in an approach (superficial) velocity of 0.0212 cm sec^{-1}.

REPLICATE BREAKTHROUGH CURVES

The following figures illustrate the duplicate (or, rarely, triplicate) breakthrough curves for each pH, ionic strength, and mineral grain treatment, which form the basis for the transport data shown in the main text. The average curves from each of the following panels, as well as the timing of several important features related to these experiments, are presented in Figure 3. Often, replicate breakthrough curves and/or average breakthrough curves cannot be discerned because they directly overlap. The abbreviation *IS* on the following panels translates to ionic strength.

Experimental conditions are also noted on each panel, with the indicated pH values being the influent pH. While the influent pH of the SLGO-bearing solutions was controlled (±0.1 s.u.)

at pH = 5.6, 7.0, and 8.3 using repeated, as-needed additions of 0.01 to 0.1 M NaOH, these systems were largely unbuffered in the column against changes in pH caused by the solutions interacting with the respective mineral coatings. As a result, the pH in the effluent of the column was consistently monitored and recorded and the authors observed that the largest change in pre-column and post-column pH occurred in high pH systems, particularly those exposed to the iron oxide coated sands. Hence, the actual pH environment within a given column is likely characterized by a gradient from the recorded influent pH to the recorded effluent pH as a function of travel distance. This phenomenon is not commonly reported in the colloid transport literature, which is likely due to either the frequent use of buffers to maintain the pH of a suspending solution or the lack of effluent pH monitoring.

The authors opted against the use of chemical buffers to maintain pH for several reasons. Due to the relatively large target range of experimental pH values utilized in this study, no single chemical buffer (e.g., Good's or bicarbonate-based buffers) could maintain the target pH against pH changes caused by the interaction between the solution and the respective mineral coatings. The use of several different chemical buffers, each with its own potential (yet generally unknown) influence on subsequent measurements would have significantly compromised the ability to isolate individual experimental variables of interest. For example, a pH 5.6, low ionic strength treatment would differ from a pH 8.3, low ionic strength treatment by not only pH, but also buffer type and ionic strength (because most Good's buffers are either Na-salts or require significant NaOH additions to achieve their effective buffering pH range, thereby altering the ionic strength). Hence, in order to accurately represent the potential range of pH conditions within a column in our systems, Figure 3 of the main text provides both the average influent and effluent pH values recorded for replicates from each treatment.

DETAILS REGARDING CONSERVATIVE TRACER EXPERIMENTS

In addition to the SLGO nanosheet breakthrough experiments described in the main text, in order to account for the internal volume of our overall flow system and specific column dispersion characteristics, we separately monitored the breakthrough of a 5 mM NaBr conservative tracer solution (λ = 218 nm) using the identical flow-through UV-vis spectrophotometer setup we previously described. We conducted NaBr tracer experiments in quartz sand for each of the six treatment conditions (i.e., three pH values by two ionic strength values). The breakthrough curves for all NaBr tracer experiments largely overlapped (Figure S4), indicating that the ionic strength and pH conditions in the associated electrolyte do not impact the conservative nature of the NaBr tracer within quartz sand columns. Hence, we averaged the NaBr tracer breakthrough curves from the quartz sand experiments and used this single curve as our basis of comparison for all treatment conditions, including the iron oxide coated sand experiments. We deemed the use of a single NaBr breakthrough curve appropriate, regardless of the sand surface coating, because the overall volume of the flow system did not change with addition of the iron oxide coated sands, as the average pore volume existing within each type of column remained constant (Section S2). In addition, we note that, in contrast to the quartz sand tracer experiments, we found that NaBr transport is significantly retarded by the positively-charged surfaces within the iron oxide coated sand columns (data not shown) indicating that NaBr is not a conservative tracer for these treatments.

ADDITIONAL DISCUSSION OF FIGURE 3 (MAIN TEXT)

In the low ionic strength quartz treatments depicted in Figure 3a (main text), the breakthrough curve for SLGO nanosheets exposed to the highest pH condition illustrates a small increase in SLGO concentration arriving at the detector, relative to the influent SLGO concentration [i.e., $C_t / C_0 > 1.0$ (up to ~1.02) from ~8 pore volumes through the end of the SLGO

transport period]. While this observation could have resulted from minor instrumental and/or analytical errors, it is reproducible (Section S3) and may suggest that a phenomenon analogous to anion exclusion is present in these systems. Under this scenario, due to the highly negative charges on both the mobile SLGO nanosheets and the stationary quartz sand mineral grains, electrostatic repulsion drives the SLGO through the column at a rate faster than advective transport would suggest. However, this increase in transport rate should be accompanied by an earlier arrival at the detector, relative to the conservative tracer, which we do not observe in this treatment. We propose that the deviation from a typical anion exclusion behavior that we see in this treatment may be caused by the gradient in pH in our columns from the influent to the effluent pH (Section S3 and Figure 3 in the main text), where exclusion occurs at the front of the column and some small degree of deposition occurs at the end of the column due to the decreasing pH. This scenario would result in a build-up of nanosheets downstream in the column, but not earlier arrival at the detector, relative to the conservative tracer. Additional elucidation of this phenomenon will require further experimentation.

REFERENCES

1. Ams, D. A., Fein, J. B., Dong, H. L., and Maurice, P. A. (2004). "Experimental measurements of the adsorption of Bacillus subtilis and Pseudomonas mendocina onto Fe-oxyhydroxide-coated and uncoated quartz grains." Geomicrobiology Journal, 21(8), 511-519.
2. Chen, C. M., Yang, Q. H., Yang, Y. G., Lv, W., Wen, Y. F., Hou, P. X., Wang, M. Z., and Cheng, H. M. (2009). "Self-assembled free-standing graphite oxide membrane." Advanced Materials, 21(35), 3541-3541.
3. Gao, W., Alemany, L. B., Ci, L. J., and Ajayan, P. M. (2009). "New insights into the structure and reduction of graphite oxide." Nature Chemistry, 1(5), 403-408.

4. Gao, Y., Li, Y., Zhang, L., Huang, H., Hu, J. J., Shah, S. M., and Su, X. G. (2012). "Adsorption and removal of tetracycline antibiotics from aqueous solution by graphene oxide." Journal of Colloid and Interface Science, 368, 540-546.

5. Hummers, W. S. and Offeman, R. E. (1958). "Preparation of graphitic oxide." Journal of the American Chemical Society, 80(6), 1339-1339.

6. Jaisi, D. P., Saleh, N. B., Blake, R. E., and Elimelech, M. (2008). "Transport of single-walled carbon nanotubes in porous media: Filtration mechanisms and reversibility." Environmental Science & Technology, 42(22), 8317-8323.

7. Li, D., Muller, M. B., Gilje, S., Kaner, R. B., and Wallace, G. G. (2008). "Processable aqueous dispersions of graphene nanosheets." Nature Nano, 3(2), 101-105.

8. Park, S. and Ruoff, R. S. (2009). "Chemical methods for the production of graphenes." Nature Nanotechnology, 4(4), 217-224.

9. Smith, J., Gao, B., Funabashi, H., Tran, T. N., Luo, D., Ahner, B. A., Steenhuis, T. S., Hay, A. G., and Walter, M. T. (2008). "Pore-scale quantification of colloid transport in saturated porous media." Environmental Science & Technology, 42(2), 517-523.

Zhang, J. L., Yang, H. J., Shen, G. X., Cheng, P., Zhang, J. Y., and Guo, S. W. (2010). "Reduction of graphene oxide via L-ascorbic acid." Chemical Communications, 46(7), 1112-1114.

SUPPLEMENTAL DATA

- Certain commercial equipment, instruments, databases, or materials may be identified in this paper to foster understanding. Such identification does not imply recommendation or endorsement by the National Institute of Standards and Technology, nor does it imply that the materials or equipment identified are necessarily the best available for the purpose.

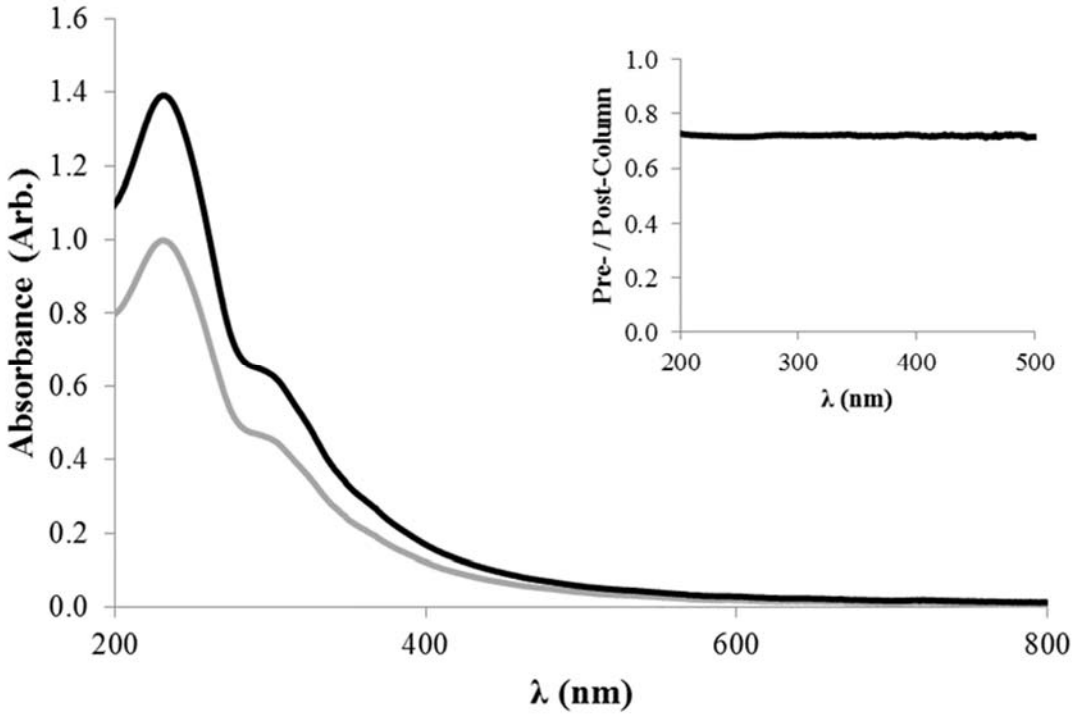

Figure S1: Typical UV-vis absorption spectra for a 25 mg SLGO L^{-1} suspension before (black) and after (grey) passing through a column packed with a porous media. This particular example is from a quartz sand experimental treatment exhibiting an ionic strength of 50 mM and an effluent pH ~5.6. The inset figure illustrates the relationship between the pre-column and post-column absorbance values, which remains constant throughout the wavelength range depicted.

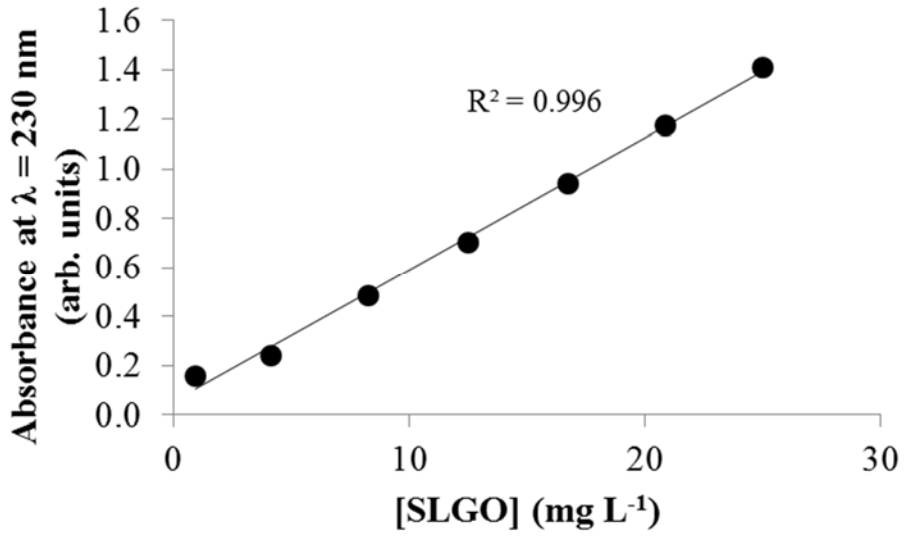

Figure S2: Regression analysis showing a linear relationship between SLGO concentration and UV-vis absorbance at λ = 230 nm.

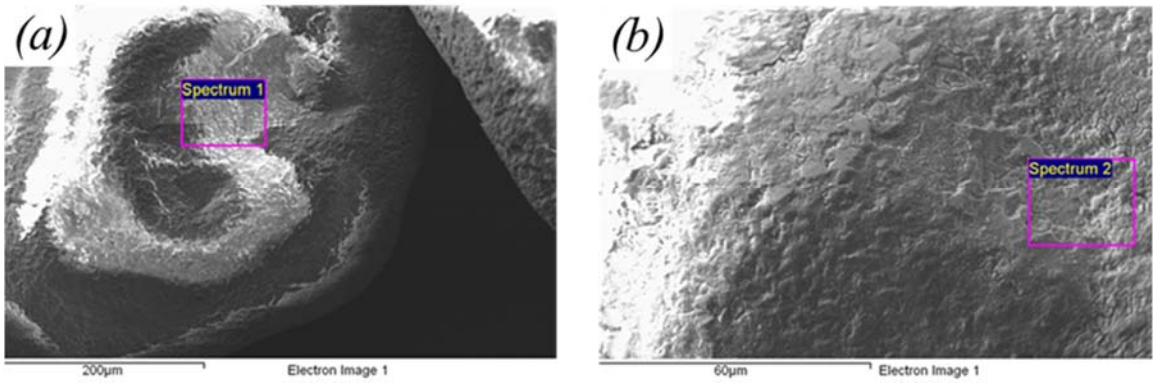

Figure S3: Representative SEM images of (a) an uncoated quartz sand grain, and (b) an iron oxide coated sand grain. Note the change in scale between the two images. EDX spectra from the indicated boxes illustrate an extensive presence of iron in (b).

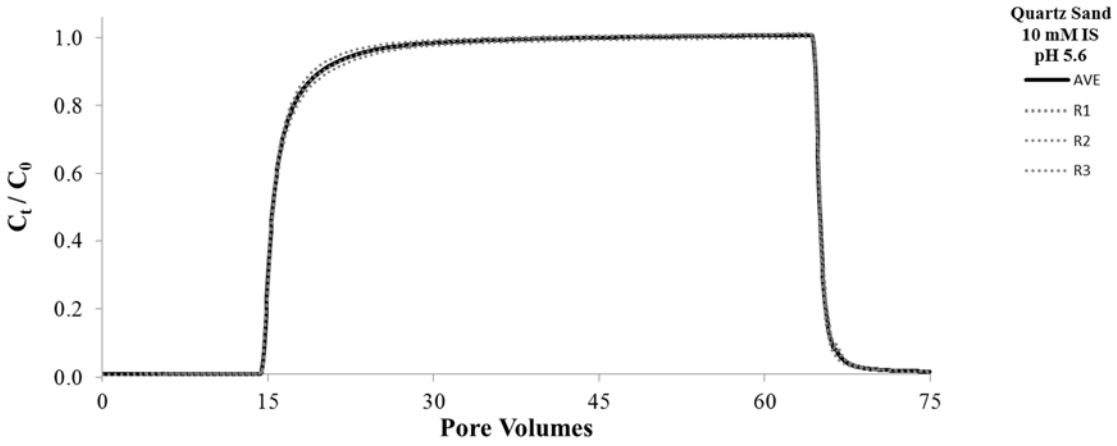
Quartz Sand
10 mM IS
pH 5.6
AVE
R1
R2
R3
C_t / C_0
1.0
0.8
0.6
0.4
0.2
0.0
0
15
30
45
60
75
Pore Volumes

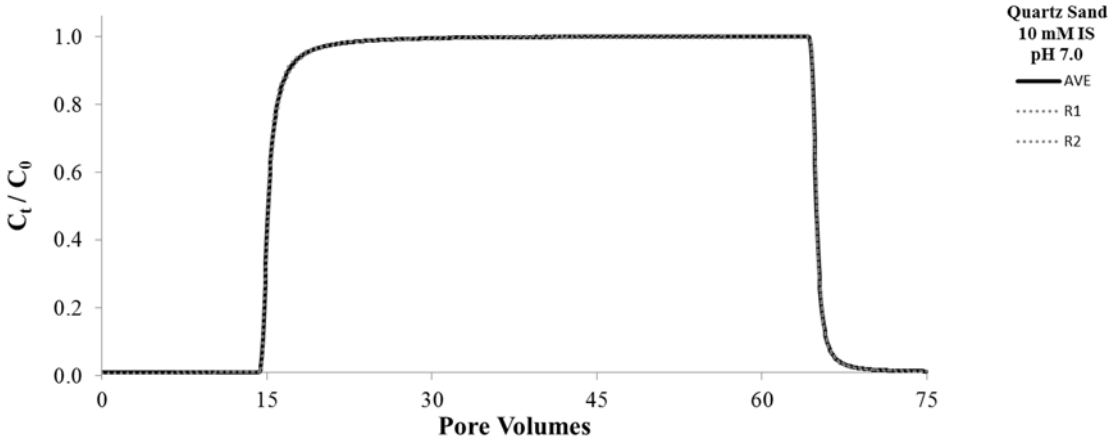
Quartz Sand
10 mM IS
pH 7.0
AVE
R1
R2
C_t / C_0
1.0
0.8
0.6
0.4
0.2
0.0
0
15
30
45
60
75
Pore Volumes

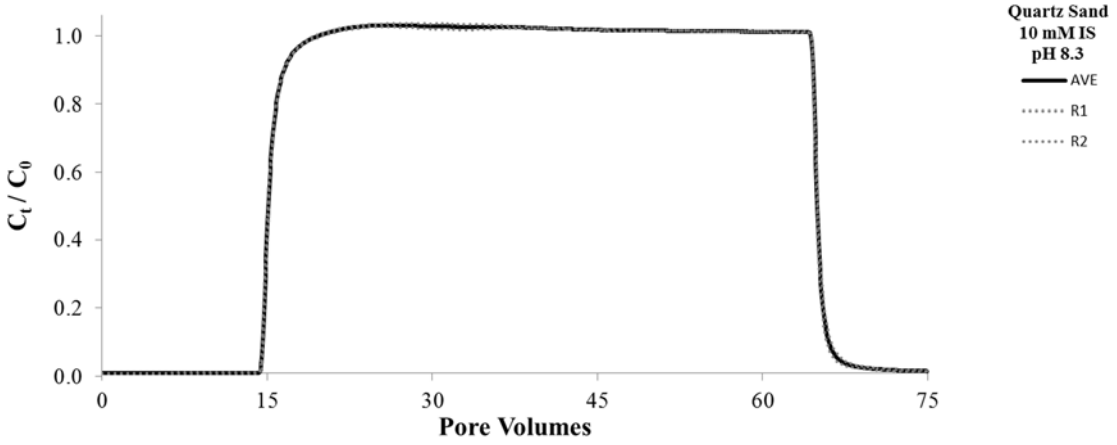
Quartz Sand
10 mM IS
pH 8.3
AVE
R1
R2
C_t / C_0
1.0
0.8
0.6
0.4
0.2
0.0
0
15
30
45
60
75
Pore Volumes

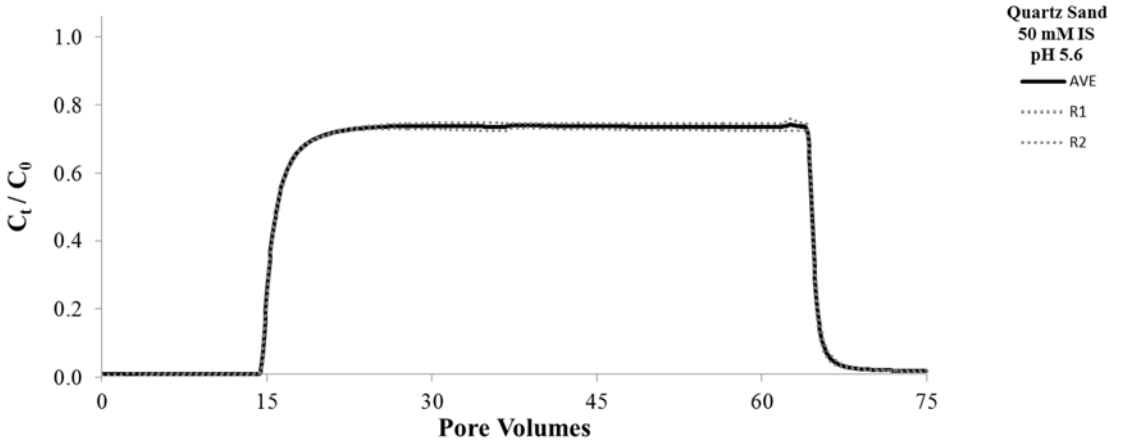
Quartz Sand
50 mM IS
pH 5.6
AVE
R1
R2
C_t / C_0
1.0
0.8
0.6
0.4
0.2
0.0
0
15
30
45
60
75
Pore Volumes

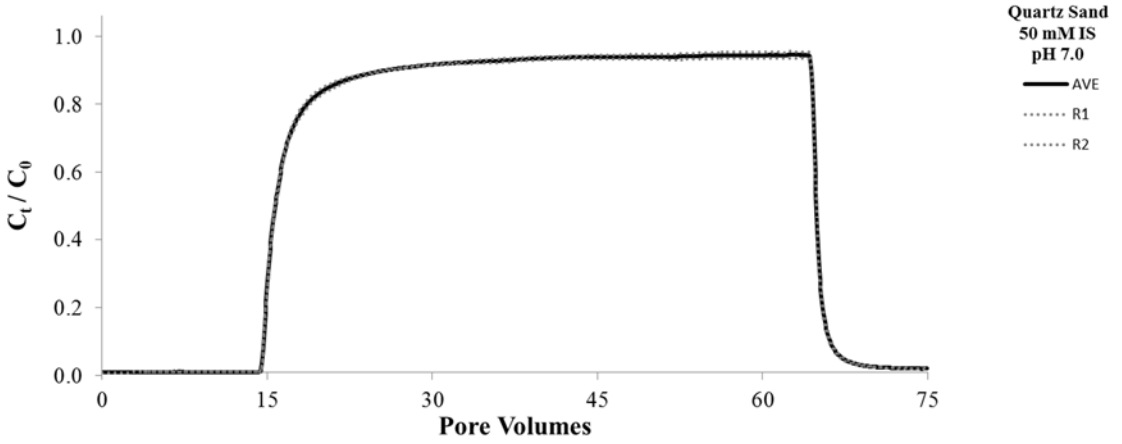
Quartz Sand
50 mM IS
pH 7.0
AVE
R1
R2
C_t / C_0
1.0
0.8
0.6
0.4
0.2
0.0
0
15
30
45
60
75
Pore Volumes

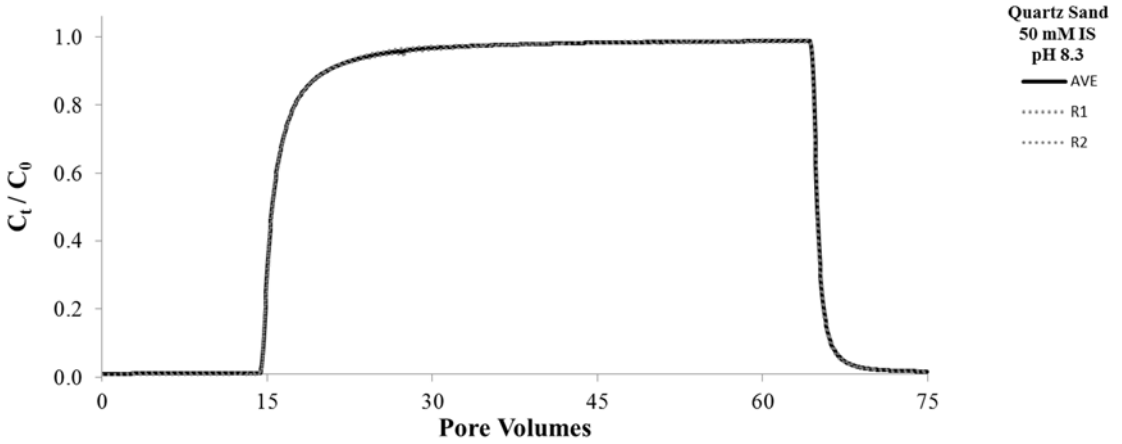
Quartz Sand
50 mM IS
pH 8.3
AVE
R1
R2
C_t / C_0
1.0
0.8
0.6
0.4
0.2
0.0
0
15
30
45
60
75
Pore Volumes

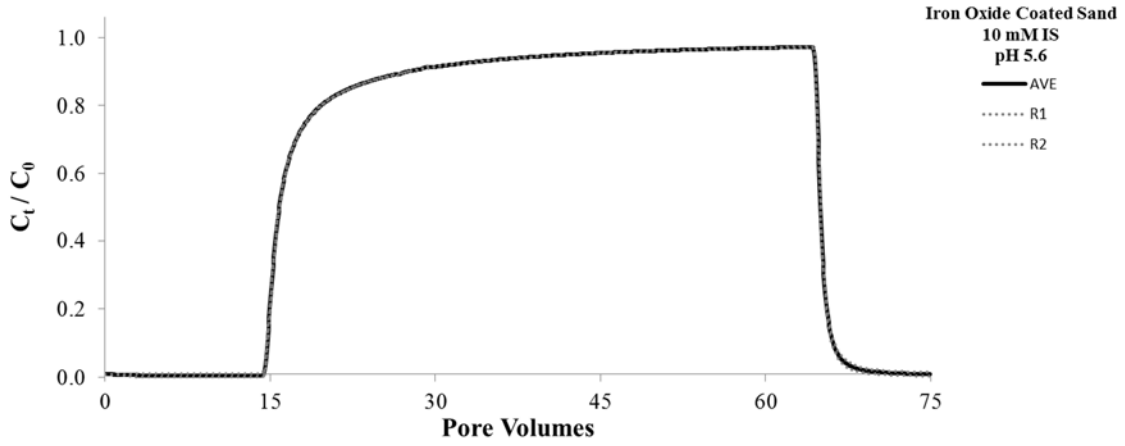
Iron Oxide Coated Sand
10 mM IS
pH 5.6
AVE
R1
R2
C_t / C_0
1.0
0.8
0.6
0.4
0.2
0.0
0
15
30
45
60
75
Pore Volumes

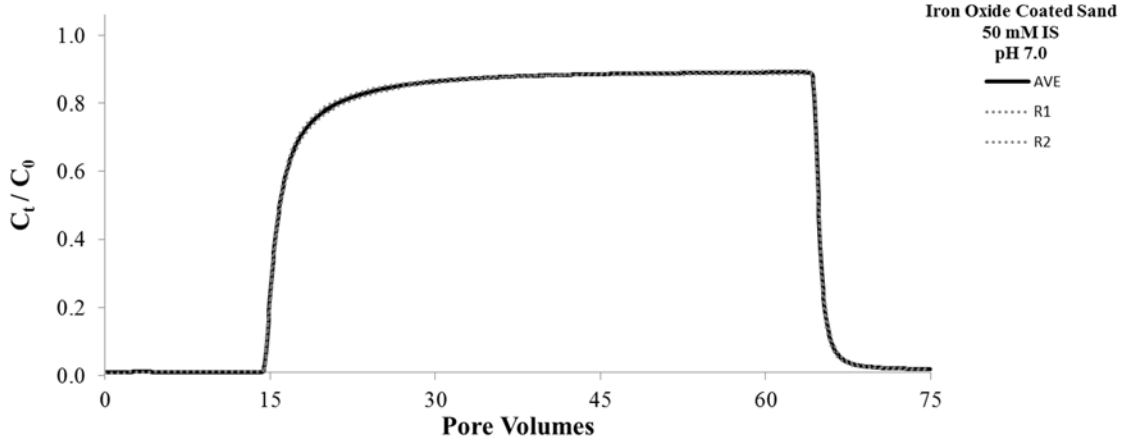
Iron Oxide Coated Sand
50 mM IS
pH 7.0
AVE
R1
R2
C_t / C_0
1.0
0.8
0.6
0.4
0.2
0.0
0
15
30
45
60
75
Pore Volumes

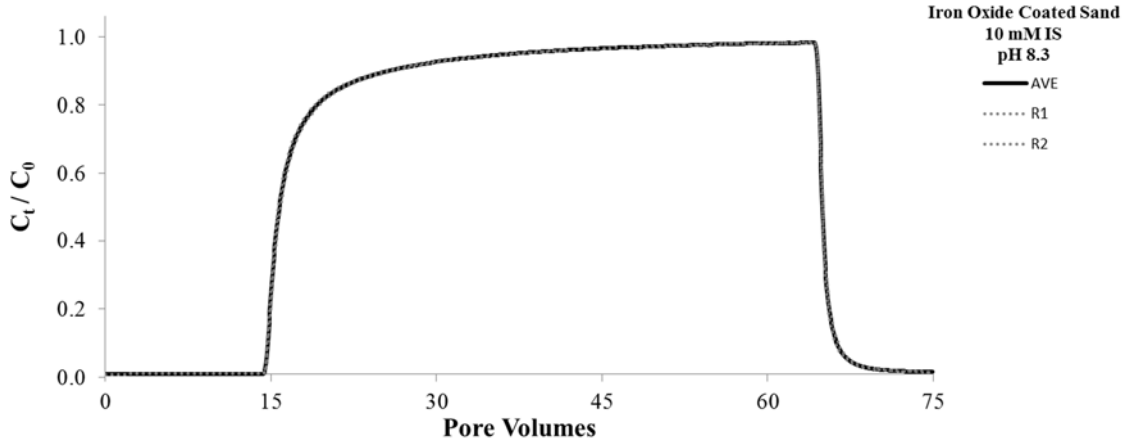
Iron Oxide Coated Sand
10 mM IS
pH 8.3
AVE
R1
R2
C_t / C_0
1.0
0.8
0.6
0.4
0.2
0.0
0
15
30
45
60
75
Pore Volumes

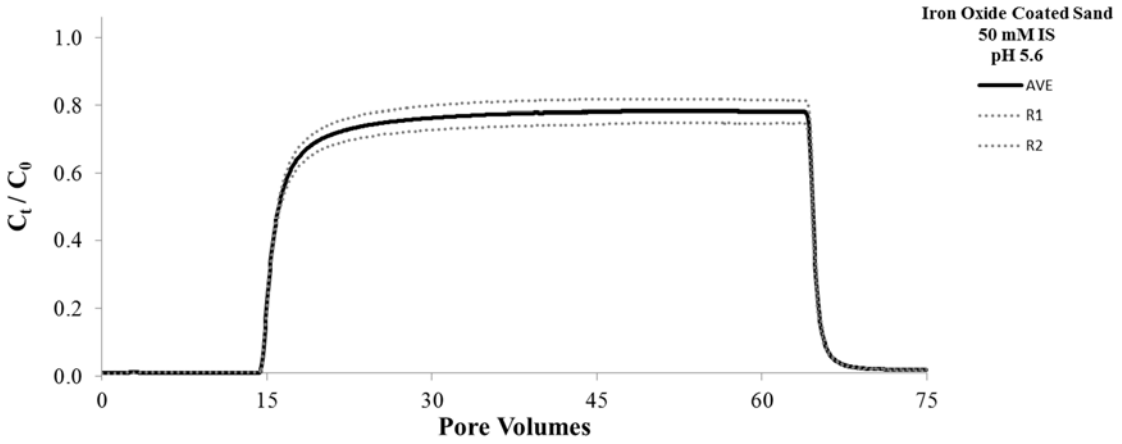
Iron Oxide Coated Sand
50 mM IS
pH 5.6
AVE
R1
R2
C_t / C_0
1.0
0.8
0.6
0.4
0.2
0.0
0
15
30
45
60
75
Pore Volumes

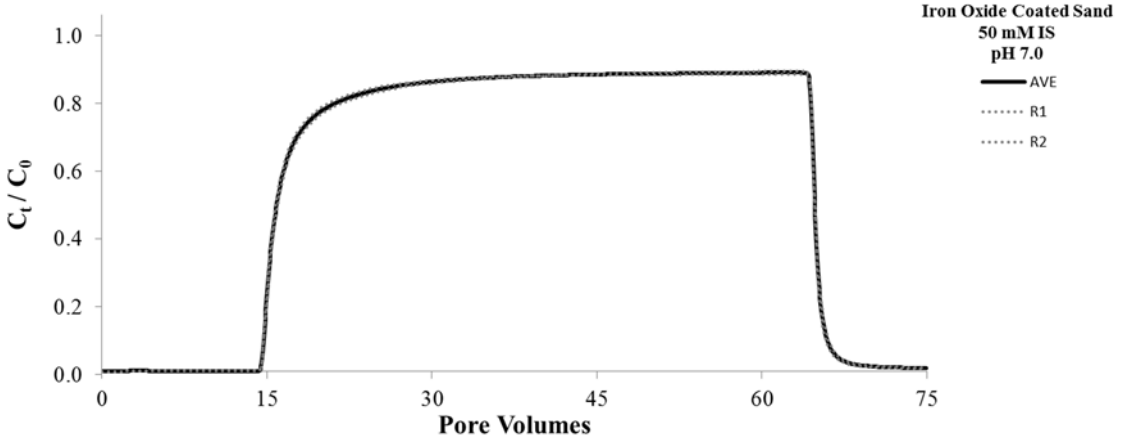
Iron Oxide Coated Sand
50 mM IS
pH 7.0
AVE
R1
R2
C_t / C_0
1.0
0.8
0.6
0.4
0.2
0.0
0
15
30
45
60
75
Pore Volumes

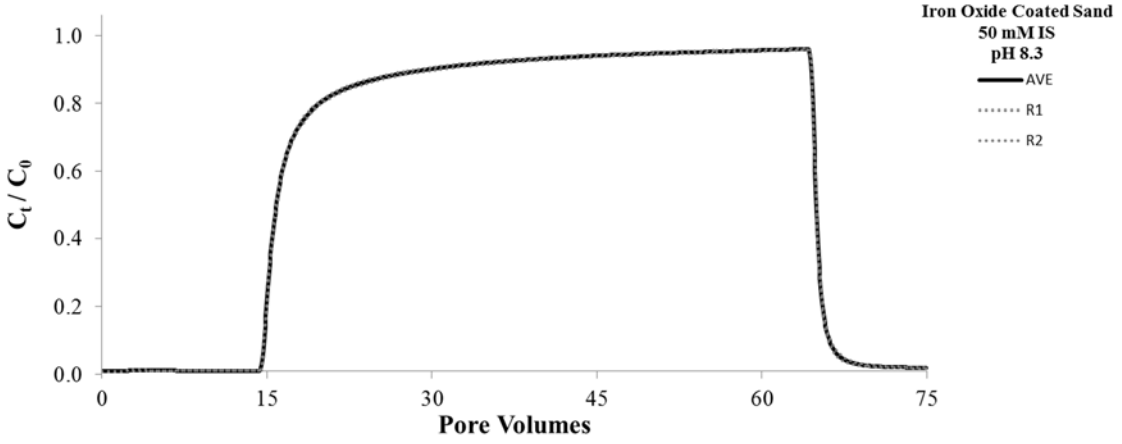
Iron Oxide Coated Sand
50 mM IS
pH 8.3
AVE
R1
R2
C_t / C_0
1.0
0.8
0.6
0.4
0.2
0.0
0
15
30
45
60
75
Pore Volumes

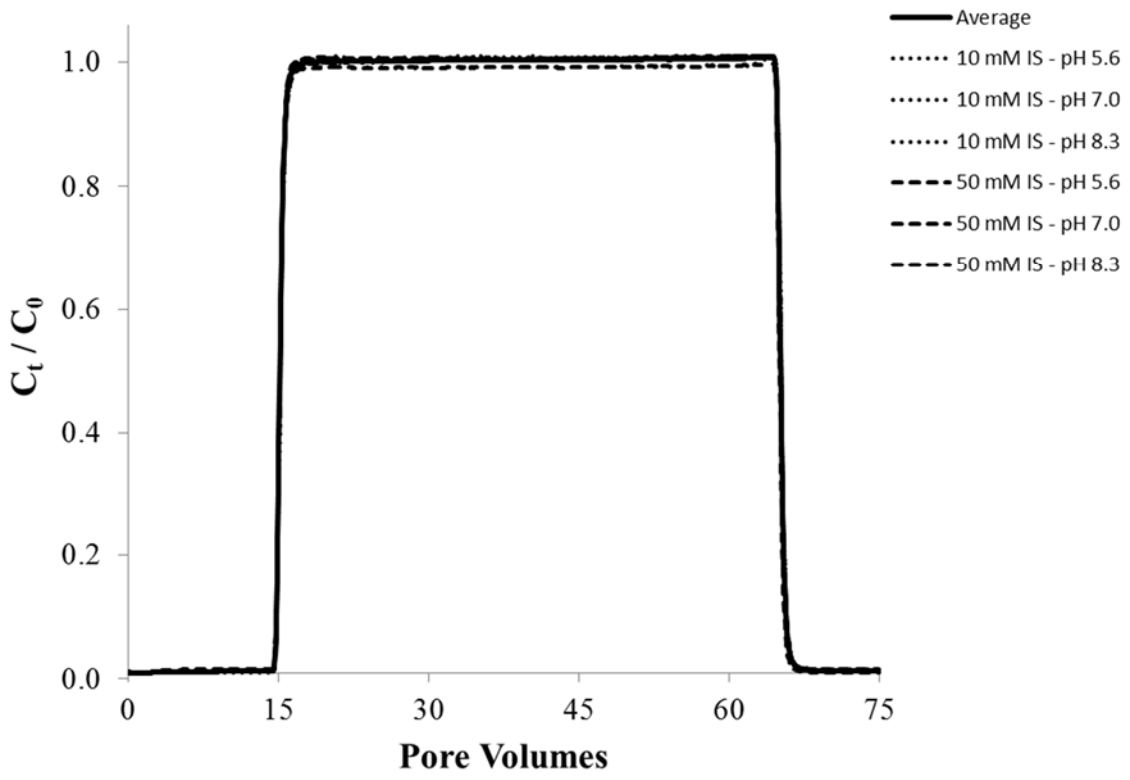

Figure S4: Breakthrough of the conservative NaBr tracer through quartz sand in the electrochemical environments listed in the figure legend. Virtually all breakthrough curves directly overlapped, so we averaged them and used this average curve for comparison to SLGO nanosheet transport, as depicted in Figure 3 in the main text.